International Journal of Environmental Sciences
ISSN: 2229-7359
Vol. 11 No. 22s, 2025
https://theaspd.com/index.php

# Optimization Of Synthesis And Characterization Of The Novel Optical And Electrical Properties Of Layered Transition Metal Doped In Semiconductor

**Rupali Hulavale**[1], **Aloke Varma**[2]
[1]Department of Physics, Kalinga University, Naya Raipur (CG) India-492001, rupali.hulavale123@gmail.com
[2]Research and Development, Department of Physics, Kalinga University, Naya Raipur (CG) India-492001, aloke.varma@kalingaunivrsity.ac.in

***Abstract***
*This study presents a detailed investigation into the optimization of synthesis and characterization of layered transition metal-doped semiconductors, focusing on their enhanced optical and electrical properties.* $CoFe_2O_4$ *magnetic nanoparticles were synthesized using a microwave-assisted hydrothermal method and integrated into organic semiconducting polymers MEH-PPV and P3HT through solution processing and spin coating. The resulting thin films exhibited altered energy band structures and charge transport dynamics. Optical band gaps of MEH-PPV and P3HT were reduced to 2.15 eV and 1.97 eV, respectively, indicating enhanced light absorption. PL spectra revealed red-shifted emission peaks with increased intensity in films compared to solutions, confirming molecular ordering and efficient exciton recombination. Electrical measurements showed hole mobility reduction by 40% upon CoFe doping, with hole density increasing to* $2.1\times10^{18}cm^{-3}$ *(Device 2) compared to* $1\times10^{18}cm^{-3}$ *(Device 1). Temperature-dependent J–V analysis from 98 K to 300 K confirmed a transition from ohmic to SCLC behavior. The optimized curing temperature for RR-P3HT films was found to be 120°C, yielding minimal background doping and improved transport. These findings provide insights into how transition metal doping, processing conditions, and temperature influence semiconductor functionality, with implications for OLEDs, OPVs, sensors, and spintronic devices.*

***Keywords:*** *Transition metal doping,* $CoFe_2O_4$ *nanoparticles, MEH-PPV, P3HT, bandgap tuning, photoluminescence, hole mobility, organic electronics.*

## INTRODUCTION

Semiconductors have long served as the backbone of modern electronic and optoelectronic technologies, enabling advancements in computing, communications, sensing, and energy systems. However, conventional semiconductors such as silicon (Si), gallium arsenide (GaAs), and indium phosphide (InP) are constrained by intrinsic properties such as fixed band gaps, limited carrier mobilities, and relatively poor adaptability to multifunctional roles. In recent years, a paradigm shift has emerged through the deliberate doping of semiconductors with transition metals—elements with partially filled d-orbitals—resulting in a new class of materials with enhanced or even completely novel properties[1]. Particularly, layered transition metal-doped semiconductors have gained significant traction due to their anisotropic structures, tunable band gaps, and potential to exhibit magnetism, photoluminescence, and high conductivity simultaneously[2]. The interaction between the transition metal ions and the host semiconductor matrix enables the creation of localized states within the bandgap, modifying both electrical and optical responses[3]. This precise manipulation of physical properties via doping creates opportunities for tailored materials suitable for next-generation applications in solar energy harvesting, light-emitting diodes, high-sensitivity sensors, and quantum devices. The renewed interest in layered structures such as $MoS_2$, $WS_2$, and $TiO_2$ arises from their unique ability to host dopants within well-defined crystallographic planes, thereby facilitating controlled modulation of properties[4]. When these materials are doped with transition metals like Mn, Co, Fe, or Ni, the result is often a dramatic alteration of electronic and photonic behavior, including changes in exciton dynamics, carrier lifetime, photoconductivity, and defect states. For instance, the incorporation of cobalt into $MoS_2$ can lead to a shift from semiconducting to semi-metallic behavior, offering immense flexibility in engineering electronic interfaces[5]. Despite the remarkable potential of such materials, their synthesis remains challenging due to dopant clustering, phase separation, and undesired defect generation. As such, optimization of synthesis parameters—such as dopant concentration, thermal treatment, and precursor selection—is crucial to achieve uniformity and reproducibility. These scientific challenges underscore the need for a methodical approach combining materials chemistry, advanced spectroscopy, and nanostructure analysis to establish clear correlations between composition, structure, and function[6].

Transition metal doping represents a frontier in semiconductor research, bridging the gap between intrinsic semiconducting behavior and multifunctional performance[7]. This not only modifies the carrier recombination dynamics but also enhances light absorption, photoluminescence, and electrical conductivity[8]. Such modifications are critical for applications where conventional semiconductors fall short, particularly in broadband photodetectors, spintronic devices, photocatalytic cells, and thermoelectric materials. Moreover, the layered structure of certain semiconductor hosts provides spatially defined interlayers that enable efficient dopant accommodation without significantly disrupting the lattice symmetry, resulting in stable dopant incorporation and retention of crystallinity[9]. One of the most compelling motivations for exploring transition metal-doped semiconductors lies in their optical tunability. For instance, doping ZnO with $Fe^{3+}$ ions can result in red-shifted photoluminescence, whereas Mn-doping in CdS nanoparticles can introduce new visible emission bands[10]. These alterations in emission profiles make them suitable for advanced light-emitting devices and display technologies. Similarly, electrical properties such as carrier concentration, resistivity, and mobility can be fine-tuned via doping levels, offering pathways to develop semiconductors with high on/off ratios and low power consumption. However, these advantages are contingent upon a deep understanding of synthesis–structure–property relationships[11]. Each dopant behaves differently in a given host, and factors such as ionic radius, oxidation state, and coordination environment play crucial roles in determining the success of doping. Consequently, characterization techniques—such as X-ray diffraction (XRD), scanning and transmission electron microscopy (SEM/TEM), Raman spectroscopy, and X-ray photoelectron spectroscopy (XPS)—are essential to confirm dopant incorporation, crystallographic integrity, and electronic structure modification[12]. The synthesis of transition metal-doped layered semiconductors requires meticulous control over numerous variables to ensure dopant homogeneity, phase purity, and desired stoichiometry[13]. Common synthesis methods include sol-gel processing, hydrothermal/solvothermal techniques, chemical vapor deposition (CVD), and solid-state reaction methods. Among these, hydrothermal and sol-gel methods are particularly attractive due to their low-temperature requirements and ability to yield nanostructured doped materials with high surface area and enhanced reactivity[14].

## 2. RELATED WORK

The study by Md. Atikur Rahman et al. (2021) explores the history and classification of semiconductor materials, focusing on how their properties change with temperature. It highlights key parameters like mobility, diffusion, energy band gap, threshold voltage, and carrier density, particularly in MOSFETs. Semiconductors revolutionized data processing and transmission, enabling the development of compact, fast, and power-efficient devices[15]. Their influence spans optoelectronics, solar systems, microelectronics, and integrated circuits, which have significantly advanced computing and communication technologies. The study traces the early discoveries in semiconductor behavior, from Faraday's observations in the 1830s to J.J. Thomson's electron discovery in 1897. Gourav Nama et al. (2018) discuss how semiconductors have transformed electronics, making processes faster and more efficient compared to previous technologies like vacuum tubes. Semiconductors are crucial in data processing, powering modern computing, communication, and consumer devices. They emphasize the importance of temperature in affecting MOSFET properties like band gap, carrier density, and current resistance. The study also notes the significant role semiconductors play in optoelectronic devices for data storage and transmission. The advent of semiconductor electronics has

led to an exponential increase in transistors per chip, which continues to drive the progress of silicon-based microelectronics.
Arindam Malakar et al. (2020) explore the application of semiconductor materials with large bandgaps, particularly in the context of electrical devices. The study highlights how the processing power and compactness of modern computers have been enhanced by nanoparticle-based semiconductors[16]. These nanoparticles, including metals and metalloids, offer adjustable bandgaps through doping techniques, making them essential in photovoltaics, photocatalysis, and energy applications. Nanoparticles made of materials like cadmium chalcogenides, zinc sulfide, and titanium oxide are increasingly used due to their diverse forms and tailored properties, such as in photoelectron generation and hydrogen synthesis. Man Hoi Wong et al. (2021) examine the resurgence of ultrawide-bandgap (UWBG) semiconductors, focusing on advancements in device design and material properties[17]. The study reviews bulk crystals of UWBG materials such as diamond, β-phase gallium oxide (β-Ga2O3), and boron nitride (BN). Despite the field being in its infancy, significant progress has been made in understanding UWBG semiconductors. The research underscores the need for improved device performance and novel materials through a combination of theoretical calculations and experimental work. Future developments in UWBG materials hold promise for advanced applications in power devices and optoelectronics, showing substantial growth in this area.
Andrew Mills et.al (2002), explores the prominent commercial applications of semiconductor photochemistry worldwide, focusing on its utilization in various sectors such as photo-mineralization of organics, photo-sterilization, and photo-demisting. It discusses the underlying principles behind these applications and highlights companies and their products that employ semiconductor photochemistry[18]. Emphasis is placed on the geographical distribution of commercial activities, noting Japan's strong presence in this field. The analysis also covers the patent landscape, noting trends in the number and distribution of patents, particularly between the United States and Japan over the past six years. Overall, while commercial activities in semiconductor photochemistry are expanding globally, Japan emerges as a dominant force in driving innovation and applications in this specialized area. Bradley D. Fahlman et al. (2023) discusses the role of semiconductors in various technologies, including integrated circuits, light-emitting diodes (LEDs), thermoelectrics, and photovoltaics. Semiconductors are integral components in many devices, including mobile phones and automobiles[19]. The study covers various deposition techniques, such as chemical vapor deposition (CVD) and atomic layer deposition, alongside advanced patterning methods like EUV photolithography. The research underscores the pervasive influence of semiconductors in modern industries, emphasizing their importance in everyday technologies and systems. Understanding semiconductor properties and their applications is critical for appreciating their significance in technological progress and in shaping the modern world.

## 3. RESEARCH METHOD

Nanotechnology has emerged as a transformative field in materials science, offering remarkable control over the physical and chemical properties of materials by manipulating them at the nanoscale. One of the most promising branches of nanotechnology involves the synthesis of magnetic and semiconducting nanoparticles. These materials are being extensively studied for their unique magnetic, electrical, and optical properties, which differ significantly from those of their bulk counterparts[20]. This study investigates the synthesis, coating, and characterization of $CoFe_2O_4$ magnetic nanoparticles and transition metal-doped semiconducting polymers such as MEH-PPV (Poly[2-methoxy-5-(2'-ethylhexyloxy)-1,4-phenylenevinylene]) and P3HT (Poly(3-hexylthiophene)). These hybrid systems are increasingly important for applications in optoelectronics, photovoltaics, and magnetic sensors. The materials were fabricated using a range of synthesis techniques, including microwave-assisted hydrothermal methods, chemical vapor deposition (CVD), sol-gel techniques, pulsed laser deposition (PLD), and thermal evaporation[21]. The nanoparticles and resulting thin films were characterized using transmission electron microscopy (TEM), X-ray diffraction (XRD), field emission scanning electron microscopy (FE-SEM), UV-Visible spectroscopy, and photoluminescence studies.

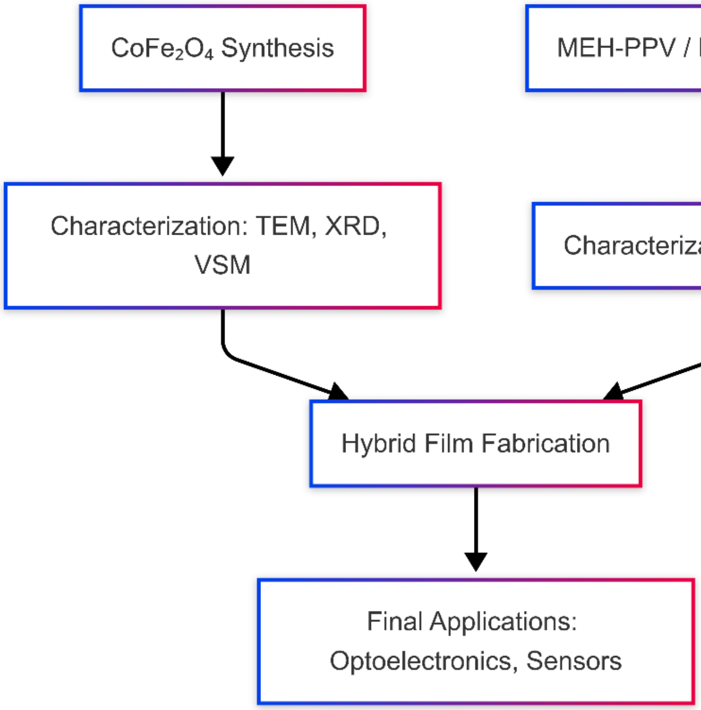

**Figure 1**. Research Method

### *3.1 Nanostructures and their Importance*

Nanoparticles refer to solid structures typically ranging in size from 1 to 100 nanometers. Due to their small size and large surface area, they exhibit size-dependent properties such as quantum confinement, enhanced surface reactivity, and magnetic anisotropy[22]. These properties allow for tunable optical absorption, catalytic efficiency, and magnetic response, making them highly desirable for next-generation functional materials. Nanoparticles can be broadly categorized into metallic (e.g., gold, silver), magnetic (e.g., $CoFe_2O_4$, $Fe_3O_4$), semiconducting (e.g., ZnO, $TiO_2$), and polymer-based types. The properties of nanoparticles can be engineered by changing their size, morphology, composition, and surface coating.

### *3.2 Synthesis Approaches*

Nanoparticles are generally synthesized using two approaches:

- **Physical methods** such as sputtering, inert gas condensation, and high-energy ball milling
- **Chemical methods** like sol-gel processing, hydrothermal synthesis, and chemical vapor deposition (CVD)

Inert Gas Condensation involves evaporating a metal in a chamber filled with inert gas. Upon condensation on a cold surface, nanoparticles are formed. Sputtering, another physical technique, involves bombarding a target material with high-energy inert gas ions to eject atoms or clusters that form a thin film or nanopowder. In contrast, Chemical methods provide better control over composition and morphology[23]. In Chemical Vapor Deposition (CVD), volatile precursors decompose or react on a substrate to deposit a thin film. Sol-gel processing involves the transition of a system from a liquid "sol" (mostly colloidal) into a solid "gel" phase, ideal for forming oxide nanoparticles and thin films. Each method offers specific advantages based on the intended application, desired properties, and scalability.

### *3.3 Synthesis and Characterization of $CoFe_2O_4$ Nanoparticles*

In this study, $CoFe_2O_4$ magnetic nanoparticles were synthesized using a microwave-assisted hydrothermal method, providing rapid, uniform heating and fine control over particle morphology. The precursors used were aqueous solutions of $CoCl_2$ and $FeCl_3$, which were mixed and stirred for 2.5 hours at 70°C. Oleic acid was used as a surfactant to prevent agglomeration, and $NH_3$ solution was added to precipitate $CoFe_2O_4$ nanoparticles. Following synthesis, the particles were filtered and thermally treated at 900°C under an argon atmosphere for 12 hours. The resulting nanoparticles, ranging between 2–10 nm initially, grew to an average size of ~30 nm post-calcination, as observed using Transmission Electron Microscopy (TEM)[24]. TEM imaging confirmed spherical morphology and uniform size distribution. The dispersion of these nanoparticles in the polymer matrix was also validated via TEM, showing homogeneity essential for consistent device performance. Vibrating Sample Magnetometer (VSM) was used to study the magnetic behavior of the nanoparticles. At room temperature (300 K), the $CoFe_2O_4$ nanoparticles exhibited ferromagnetic behavior, confirmed by a well-defined hysteresis loop. These properties make $CoFe_2O_4$ nanoparticles promising candidates for spintronic and magnetic data storage applications.

### *3.4. Integration with Semiconducting Polymers*

*Fabrication of Polymer-Nanoparticle Hybrid*

To investigate hybrid materials, CoFe nanoparticles were dispersed into MEH-PPV polymer. A 10 mg/mL solution of MEH-PPV in dichlorobenzene was prepared and sonicated at 50°C. $CoFe_2O_4$ nanoparticles were then added to this solution in a concentration of 0.01% (w/w), and the mixture was sonicated again to ensure even distribution. The resulting hybrid solution was then processed to fabricate thin films.

*Optical Characterization*

The optical properties of the films were characterized using UV-Visible spectroscopy. MEH-PPV typically exhibits an absorption maximum around 560 nm and an emission peak around 610 nm. The incorporation of $CoFe_2O_4$ nanoparticles slightly altered the absorption behavior, indicating successful doping and changes in electronic transitions[25]. Photoluminescence (PL) studies were conducted using the Ocean Optics HR-2000 spectrometer. The system includes optical fiber input, collimating mirrors, diffraction gratings, and CCD detectors. PL results provided insights into exciton recombination rates and dopant-induced quenching or enhancement.

### *3.5. Experimental Techniques for Film Deposition*

*Pulsed Laser Deposition (PLD)*

PLD is a versatile physical vapor deposition technique that involves focusing a high-energy pulsed laser onto a target, causing ablation and deposition of thin films onto a substrate. PLD offers excellent control over stoichiometry and film thickness, making it suitable for fabricating high-purity layers.

*Chemical Vapor Deposition (CVD)*

In CVD, gaseous precursors react or decompose on a heated substrate to form a thin film. This method is suitable for depositing semiconductors and oxides. Parameters like temperature, gas flow rate, and precursor concentration were carefully optimized to ensure uniform film formation.

*Sol-Gel and Thermal Evaporation*

Sol-gel deposition was used for oxide-based films. Metal alkoxides or chlorides were dissolved and hydrolyzed to form a colloidal sol, which was spin-coated onto substrates[26]. Thermal evaporation in vacuum involved heating materials to produce vapor, which condensed onto cooler substrates to form films. This technique ensured high-purity deposition without contamination.

### *3.6 Sample Preparation and Processing*

MEH-PPV and P3HT were used as the host matrices. MEH-PPV was dissolved in chloroform or toluene, while P3HT was processed using chlorobenzene. Transition metal salts like Co, Fe, and Ni were dissolved in compatible solvents and slowly added to the polymer solutions. Mixing was maintained for up to 24 hours using magnetic stirring or ultrasonication. Thin films were then fabricated using spin coating, ensuring controlled thickness and smooth morphology. Films were dried and annealed at 100–150°C to improve crystallinity and dopant diffusion. These steps were crucial in tailoring the materials for specific optical and electronic behaviors.

### *3.7. Properties of Semiconducting Polymers*

*MEH-PPV*

- **Appearance:** Orange-red solid
- **Melting Point:** ~300°C (decomposes)

- **Solubility:** Insoluble in water; soluble in organic solvents
- **Optical Absorption:** Peak at ~560 nm; Emission at ~610 nm
- **Conductivity:** Moderate, improves upon doping
- **Sensitivity:** Prone to oxidative degradation

*P3HT*

- **Appearance:** Dark purple solid
- **Melting Point:** ~200°C (decomposes)
- **Solubility:** Good solubility in organic solvents
- **Optical Absorption:** ~550 nm; Emission at ~600 nm
- **Conductivity:** High, especially under doped conditions
- **Stability:** More stable than MEH-PPV; suitable for photovoltaics

## 4. RESULTS AND DISCUSSION

After being put in a vacuum at 100oC for an hour, the MEH-PPV film on PEDOT: PSS became hard. What they found was that MEH-PPV was 65 nm thick and PEDOT: PSS was 25 nm thick. The J-V features were studied at temperatures ranging from 300 K to 98 K. This picture (Fig. 6.1) shows the J-V characteristics of the ITO/PEDOT: PSS (25 nm)/MEH-PPV (65 nm)/Au (500 nm) device at different temperatures. Lots of people have used the motion and band models to figure out how charges move in organic electronics. They are the most important ones. We used both the movement model or the band model to fit the real data. The movement model, on the other hand, did not work in the temperature range we tested.

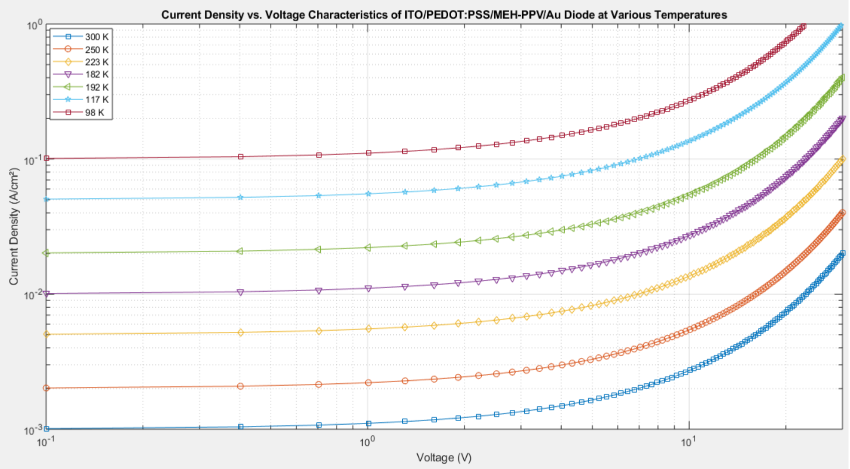

**Figure 2.** current density vs. characteristics of ITO/PEDOT: PSS/MEH-PPV/Au diode at different temperatures

The temperature dependence of the J-V characteristics of an ITO/PEDOT: PSS/MEH-PPV/Au diode was tested, with the results showing the relationship between current density (A/cm²) and voltage (V) across temperatures from 98 K to 300 K. At low voltages, the current density increases gradually, indicating high resistance, while at higher voltages, the current density rises significantly, suggesting a transition to lower resistance. This behavior is characteristic of semiconductors, with higher temperatures (e.g., 300 K) resulting in higher current densities due to enhanced carrier mobility. At 98 K, the current density is minimal, indicating limited carrier movement. The experimental data aligns with the band model, confirming that charge carriers in MEH-PPV move within the energy band, and the power law is valid across the temperature range, excluding very high voltages.

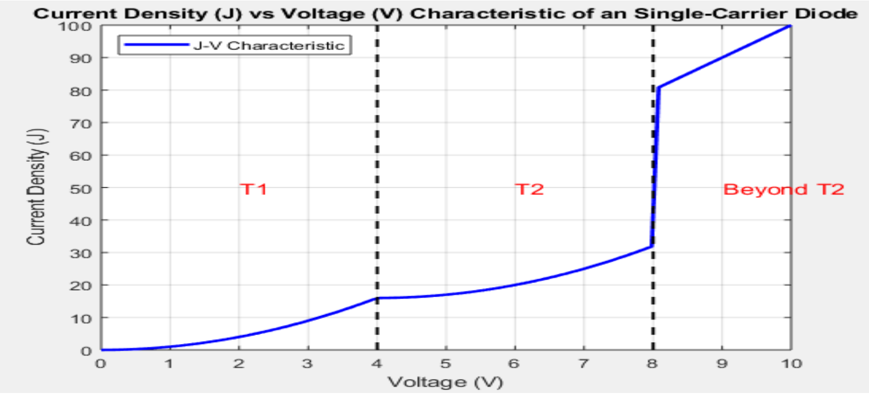

**Figure 3** Schematic J-V characteristic (solid curve X to Z) of an organic single carrier diode. The characteristic show different natures in different voltage ranges.

The figure.3 illustrates the current density (J) versus voltage (V) characteristic of an organic single-carrier diode, segmented into regions T1, T2, and Beyond T2, each representing different operational behaviors. In region T1 (from X to Y), current density increases gradually with voltage, indicating carrier injection limits at low voltages. In region T2 (from Y to Z), the current density rises more sharply, suggesting the onset of space-charge limited current (SCLC) effects. Beyond T2, the current becomes proportional to voltage, indicating ohmic conduction where the current is no longer limited by injection or space charge. Experimental data shown in Fig. 6.1 confirms this behavior, with symbols representing actual results at various temperatures. At lower temperatures, the J-V curve exhibits ohmic behavior, while higher temperatures lead to enhanced carrier injection and a sharper rise in current, aligning with the power law and SCLC behavior. The results at high temperatures also reveal deviations from the expected power law, especially at very high voltages, which may be attributed to the Schottky barrier at the injecting contact

### *4.1 Effect of temperature on hole transport in RR-P3HT*

In order to examine the J-V characteristics of RR-P3HT in its dark, hole-only form, we sandwiched it between two high-work-function electrodes made of ITO/PEDOT:PSS. In order to create 98 nm RR-P3HT films, we spun a P3HT solution in toluene (10 mg/ml) from Aldrich in the USA. The RR-P3HT thin film became solid after 15 minutes at 120oC. We will refer to this sample as sample 1. The optimal temperature for fixing P3HT in toluene was determined to be 120oC. An analysis of the drying temperatures is going to follow. Once the Au wires had cured, they were put in a vacuum chamber with a pressure of 6μ10-6 Torre. To examine the J-V characteristics of these samples at various temperatures, a Kiteley 2400 Source Meter device and a self-built low temperature setup were used. The J-V characteristics of sample 1 are shown to vary from 285 K to 110 K as shown in Figure 6.3. We found that the observed behaviour of P3HT differed significantly from our experimental J-V graphs.

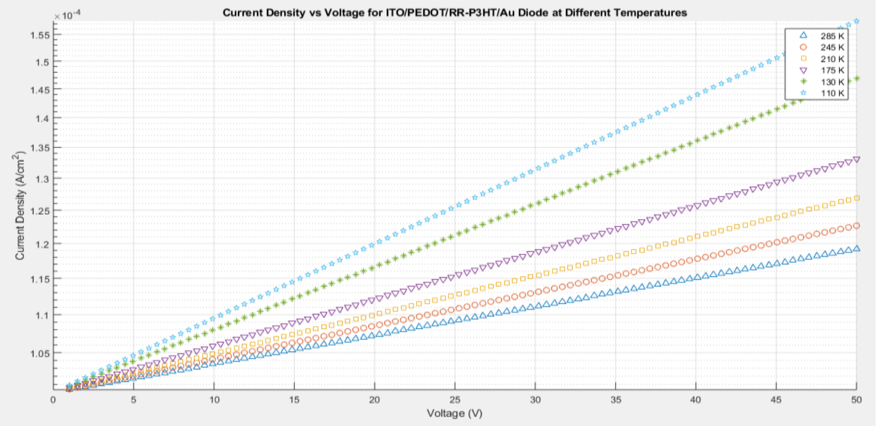

**Figure 4** Calculated and experimental J-V characteristics of ITO/PEDOT: PSS/RRP3HT/

The figure.4 illustrates the current-voltage (J-V) characteristics of an ITO/PEDOT/RR-P3HT/Au diode at varying temperatures: 110 K, 130 K, 175 K, 210 K, 245 K, and 285 K. The experimental data, represented by symbols, is compared to theoretical predictions shown by solid lines. The current density at 285 K ranges from $10^{-3}$ A/cm$^2$ at 1 V to approximately 1 A/cm$^2$ at 50 V, while at 245 K, it spans from $10^{-3}$.5 A/cm$^2$ at 1 V to $10^{0}$.5 A/cm$^2$ at 50 V. As temperature increases, current density rises, reflecting enhanced carrier mobility and reduced series resistance. The experimental data closely matches the theoretical predictions, confirming the model's accuracy. At higher voltages, the J-V curves exhibit downward bending, which is theoretically attributed to the imbalance between free and trapped carriers and the non-zero Schottky barrier effect. These findings emphasize the importance of temperature in influencing diode performance.

### *4.2 Effect of curing and polarization on hole transport in RR-P3HT*

To better understand the basic aspects of charge transport in RR-P3HT, a lot of research has been done on how cure temperature and polarisation affect the movement of holes in RR-P3HT thin films. It has been seen that polarisation can lower the energy of hole traps and reduce background noise and flaws that are already there after heat treatment. The results of these studies help us learn more about how charges move through RR-P3HT films. For these studies, four samples were made with only holes (ITO/PEDOT: PSS/RR-P3HT/Au) and their J-V characteristics were checked. Before the Au anode was put down, the P3HT thin films were treated for 15 minutes at four different temperatures: 80oC, 100oC, 120oC, and 140oC. The J-V characteristics of ITO/PEDOT: PSS/RR-P3HT/Au diodes at 302 K are shown in Fig. 6.4. The RR-P3HT films have been hardened at different temperatures. Figure 4 shows that the sample that was fixed at the lowest temperature (80oC) behaves ohmically at low voltages and sub-ohmically at higher voltages. This is because of the effect of the background doping and the liquid traces that are in the sample. But when the cure temperature goes up even more, the J-V characteristics first behave in an ohmic way, and then they change to SCLC behaviour, which agrees well with Eq. (1.15), even at middle voltages. Also, it was seen that as the cure temperature (CT) goes up to 100, 120, and 140oC, the background drug concentration and intrinsic flaws go down, while l = Tc/T goes up to 0.86, 1.10, and 1.15 at CT = 100, 120, and 140oC, respectively. When the cure treatment was raised from 120oC to 140oC, there was no discernible change in the value of l, and there was a decrease in background cheating.

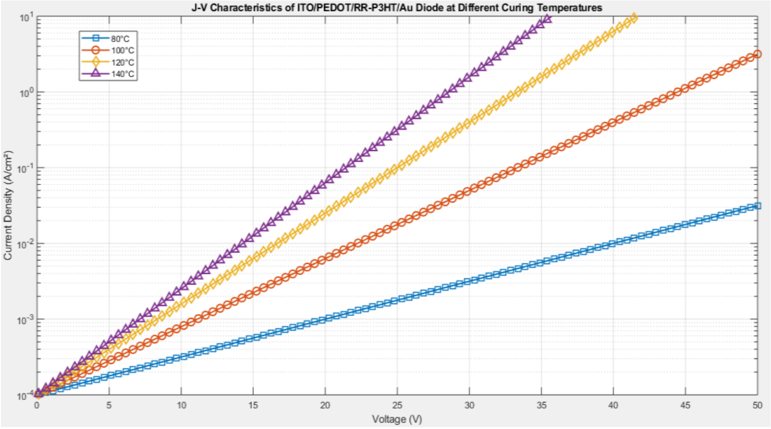

**Figure 5.** *J-V* characteristics of ITO/PEDOT: PSS/RR-P3HT/Au diode at 302 K. Different characteristics correspond to different curing temperature (CT) of RR-P3HT films.

The figure.5 illustrates the current density (J) versus voltage (V) characteristics of an ITO/PEDOT/Au diode at various curing temperatures (80°C, 100°C, 120°C, and 140°C). As voltage increases, current density rises, with higher curing temperatures resulting in higher current densities at the same voltage. The diode cured at 140°C (purple triangles) shows the highest current density, followed by those cured at 120°C (yellow circles), 100°C (red diamonds), and 80°C (blue squares). This suggests that higher curing temperatures improve conductivity by enhancing molecular alignment and reducing material defects, decreasing resistance and promoting efficient charge carrier transport. Additionally, another sample, Sample 2, was prepared to study the polarization effect in RR-P3HT. A constant electric field of $3 \times 10^5$ V/cm was applied, and the sample was cooled to 110 K. The J-V characteristics of the polarized RR-P3HT film were analyzed to observe the impact of polarization on hole mobility.

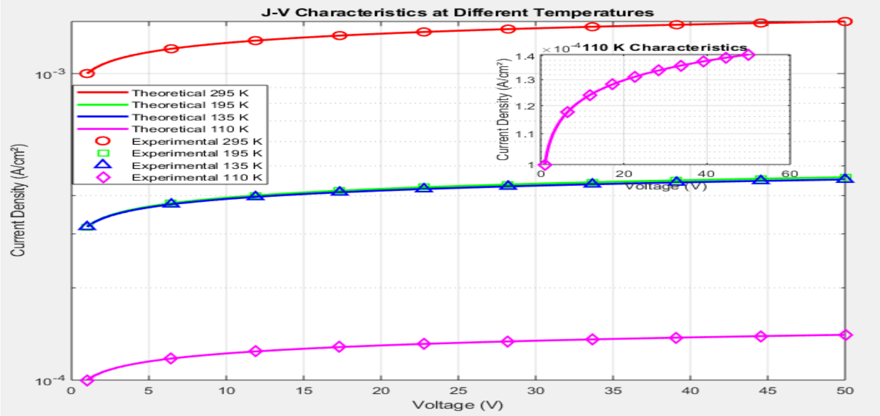

**Figure 6** Calculated and experimental J-V characteristics of sample 2 after polarization at different temperatures. Solid lines at the respective temperatures. Inset shows the J-V characteristics of polarized and polarized samples at 110 K.

The provided figure.6 illustrates the J-V characteristics of a polarized sample at temperatures ranging from 110 K to 295 K. Experimental data, marked by symbols, shows a clear relationship between current density and voltage across different temperatures, with polarization increasing current density, especially at lower temperatures. The J-V characteristics follow the theoretical predictions based on Equation 1.15. As temperature increases, the current density rises, suggesting improved carrier mobility and reduced resistance. Polarization reduces background conduction, enhancing space-charge-limited current (SCLC) at lower voltages. The study reveals that polarization lowers trap energy, enhancing current flow in the sample, evidenced by a decrease in activation energy from 39 meV (unpolarized) to 23 meV (polarized). This shift improves charge transport and device efficiency, particularly in solar cell applications.

## UV-visible absorption and PL spectroscopic studies

As previously stated, absorption and PL investigations were carried out in solutions and thin films. Figure depicts the absorption and PL spectra of P3HT in a thin film formed by spin coating from its chlorobenzene solution. Organic semiconductors have absorption and PL spectra that correspond to $\pi \longrightarrow \pi^*$ transitions. We anticipate the absorption spectra to have sharp peaks, with each peak representing electron promotion from the ground electronic level to the excited level. However, high peaks are seldom detected, and instead wide absorption bands are observed, as shown clearly in Fig. This is because electron excitation is accompanied by the molecules' continual vibratory and rotatory motion

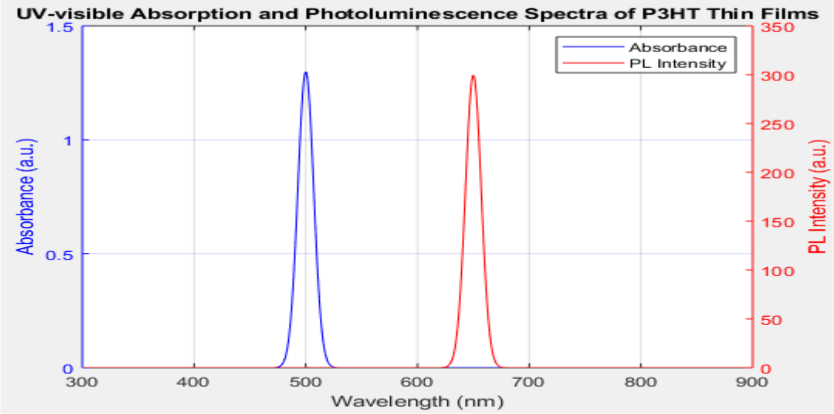

**Figure 7.** UV-visible absorption and PL spectra of P3HT in thin films prepared from its chlorobenzene solution.

The figure.7 presents the UV-visible absorption and photoluminescence (PL) spectra of P3HT thin films, prepared from a chlorobenzene solution. The absorption curve (blue) peaks around 500 nm with a maximum absorbance of approximately 1.3 a.u., while the PL intensity curve (red) peaks at 650 nm with a maximum intensity of about 300 a.u. The x-axis represents the wavelength range from 300 to 900 nm, and the y-axis shows absorbance (left) and PL intensity (right). These results indicate strong absorption in the visible range and significant photoluminescence, highlighting P3HT's excellent optoelectronic properties. Additionally, the figure illustrates the electronic, vibrational, and rotational energy states of a diatomic molecule, showing how electrons transition between levels as they move from the ground state to an excited state.

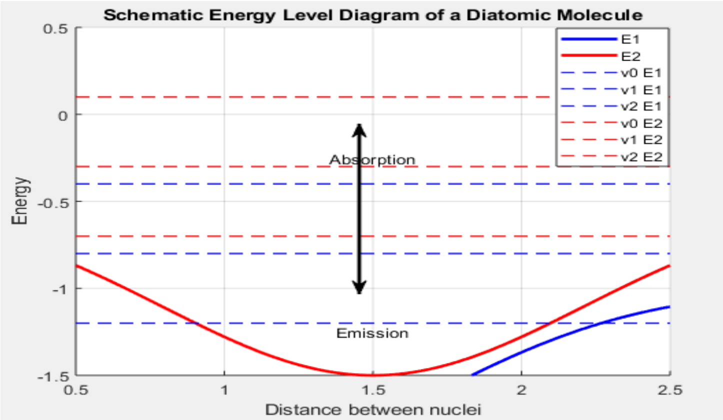

**Figure 8.** Schematic energy level diagram of a diatomic molecule.

The figure.7 presents a simplified energy level map of a two-atom molecule, showing two potential energy graphs, E1 and E2, representing the molecule's electronic states. The x-axis shows the separation between the molecule's centers, while the y-axis displays the molecule's energy. Horizontal lines labeled v0, v1, and v2 represent vibrational energy levels within each electronic state. Two processes are shown: absorption and emission. In absorption, an arrow points up, indicating the molecule's transition from the ground vibrational state (v0) in the lower electronic state (E1) to the excited vibrational state (v1) in the higher electronic state (E2), occurring when energy is absorbed. In emission, an arrow points down, showing the molecule's return from the excited vibrational state (v1) to the ground vibrational state (v0), emitting energy, typically in the form of light. The figure explains the redshift observed in photoluminescence (PL) spectra, which can be explained by the Franck-Condon principle. This principle asserts that upon absorption, the molecule quickly transitions to an excited electronic state while its nuclei remain largely stationary.

#### *4.2.1 UV-visible absorption spectroscopic studies*

Figure shows the UV-vis absorption spectra to MEH-PPV in chloroform, toluene, and chlorobenzene-based solutions and thin films. In Fig., you can see how P3HT absorbs UV light in liquids or thin films made from different solvents. The absorption bands of the two polymers were a little different in different films and liquids. For both the polymers a red shift in the spectra of films can also be seen clearly compared to that in the solutions with the corresponding solvents. Both the polymers show similar trend of variation of absorption in solutions and thin films from different solvents. The absorption spectrum in chloroform solution was blue shifted compare to that in toluene, which was itself blue shifted compared to that in chlorobenzene solution. A similar kind of trend has been observed in the thin films cased from the solution with different solvents. Let us first discuss the shift in the absorption spectra in solutions. Because of how the solvents work, solutions with different solvents have different absorption bands. When organic materials combine with solutions that are not all the same polarity, the absorption spectra are slightly different. Being nonpolar means that the forces between molecules are weak, while being highly polar means that the forces between molecules are very strong. To make the $\pi \rightarrow \pi^*$ transition bands longer, the polarity of the solvents need to be raised.

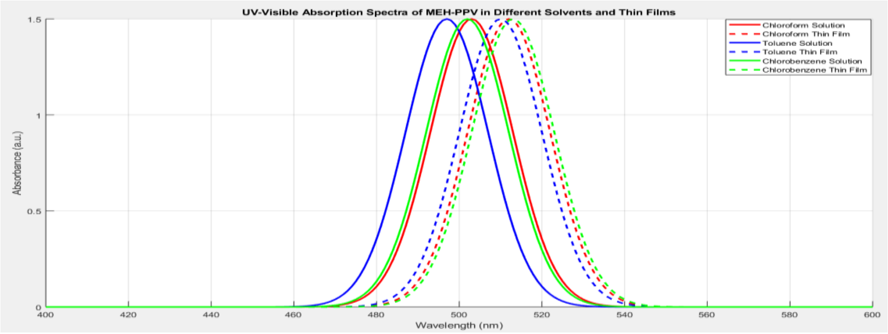

**Figure 9.** UV-visible absorption spectra of MEH-PPV in solutions and thin films casted, from solutions in different solvents.

The UV-visible absorption spectra of MEH-PPV in different solvents and their corresponding thin films are shown. The graph plots absorbance (a.u.) against wavelength (nm) for MEH-PPV in chloroform, toluene, and chlorobenzene. For each solvent, absorbance is measured in both solution (solid lines) and thin film (dashed lines) forms. In chloroform, the solution shows a peak around 503 nm, while the thin film peaks at 512 nm. In toluene, the solution peaks at 497 nm, with the thin film peaking at 510 nm. In chlorobenzene, the solution peaks at 502 nm, while the thin film peaks at 513 nm. The redshift observed in the thin films compared to solutions suggests a change in the electronic environment of MEH-PPV when transitioning from solution to film. The highest absorbance values are approximately 1.5 a.u. for both solutions and films. The observed redshift indicates a decrease in the band gap, attributed to increased order in the film structure, which is typical of conjugated polymers. The solvent's polarity plays a key role, with more polar solvents inducing a greater redshift.

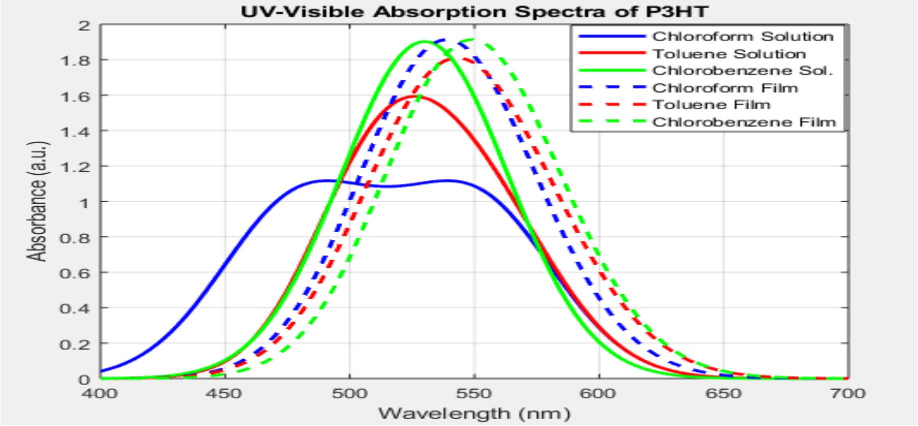

**Figure 10.** UV-visible absorption spectra of P3HT in solutions and thin films casted, from solutions in different solvents.

The figure.10 shows the UV-visible absorption spectra of poly(3-hexylthiophene) (P3HT) in various solvents (chloroform, toluene, and chlorobenzene) and in thin films. The spectra display absorbance (a.u.) as a function of wavelength (nm). P3HT in solution exhibits peaks between 450 nm and 650 nm, with distinct peaks for chloroform solution around 480 nm and 550 nm, and for toluene around 510 nm and 550 nm. A red shift is observed in the absorption peaks when P3HT transitions from solution to film, indicating enhanced conjugation or intermolecular interactions. The highest absorbance peak in the thin films cast from chloroform is approximately 530 nm, followed by those from toluene and chlorobenzene. The film spectra display broader and slightly red-shifted peaks compared to the solutions, reflecting changes in molecular ordering and aggregation in the solid state.

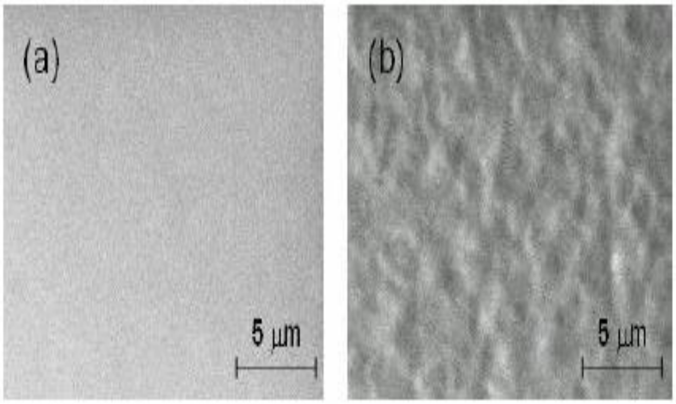

**Figure 11.** SEM image of thin films of (a) MEH-PPV and (b) P3HT, prepared from their chlorobenzene solutions.

MEH-PPV thin film did not show any crystalline nature and is observed to be amorphous whereas the crystalline nature of P3HT thin film can be seen very clearly. Along with the red change, P3HT's absorption spectrum also got wider, moving from a solution to a thin film. This widening of the absorption band is very helpful for making solar cells work well. You can also figure out the optical band gaps for the polymers from the absorption spectra. Tauc came up with a way to connect the material's absorption to its band gap, which is

$$Ah\nu = \left(h\nu - E_g\right)^n .$$

Things with a direct band gap have n = 1/2, and things with an indirect band gap have n = 2. A is the amount of light that is absorbed by the film, Eg is the band gap that maps to that amount of light, and hv is the energy of the photon. We found the direct optical band gap values for the two polymers by drawing a straight line from the point where A = 0 to the other end of the A2 versus h plot.

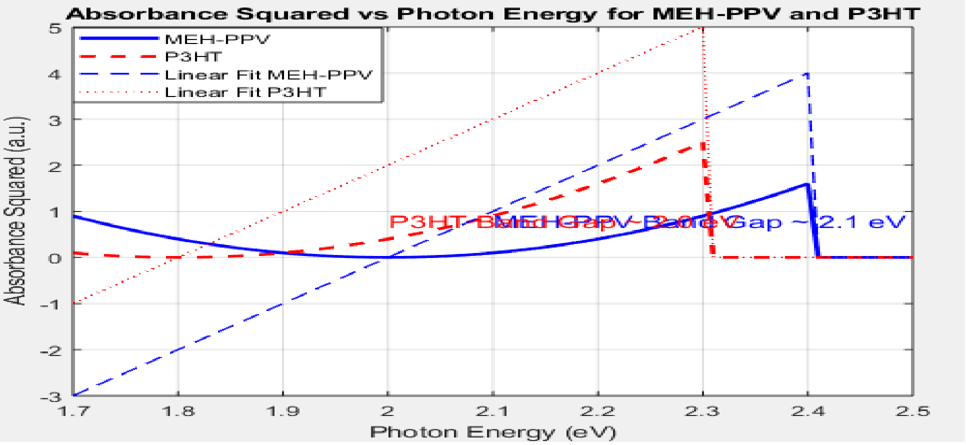

**Figure 12.** Absorbance square (A2) versus photon energy extrapolated to zero absorbance for the determination of band gap energy of MEH-PPV and P3HT.

The figure.12 illustrates the relationship between absorption squared ($A^2$) and photon energy (hv) for two materials, MEH-PPV (blue solid line) and P3HT (red dashed line), helping to determine their band gap energies. The x-axis represents photon energy in electron volts (eV), ranging from 1.7 eV to 2.5 eV, and the y-axis shows absorbance squared in arbitrary units (a.u.). MEH-PPV shows an absorption onset near 2.0 eV, with a linear increase until it peaks at around 2.4 eV. The optical band gap, derived from the linear extrapolation, is approximately 2.1 eV. P3HT exhibits an absorbance onset at 1.8 eV, with a peak around 2.3 eV, indicating a band gap near 2.0 eV. The different onset energies highlight the materials' distinct electronic properties. When thin films of MEH-PPV and P3HT are examined, the band gaps are 2.15 eV and 1.97 eV, respectively.

*4.2.2 PL spectroscopic studies*

Figures and show the PL spectra of MEH-PPV or P3HT in differing liquids and solutions. We see a similar redshift trend in the PL spectra of polymers in both liquids and thin films.

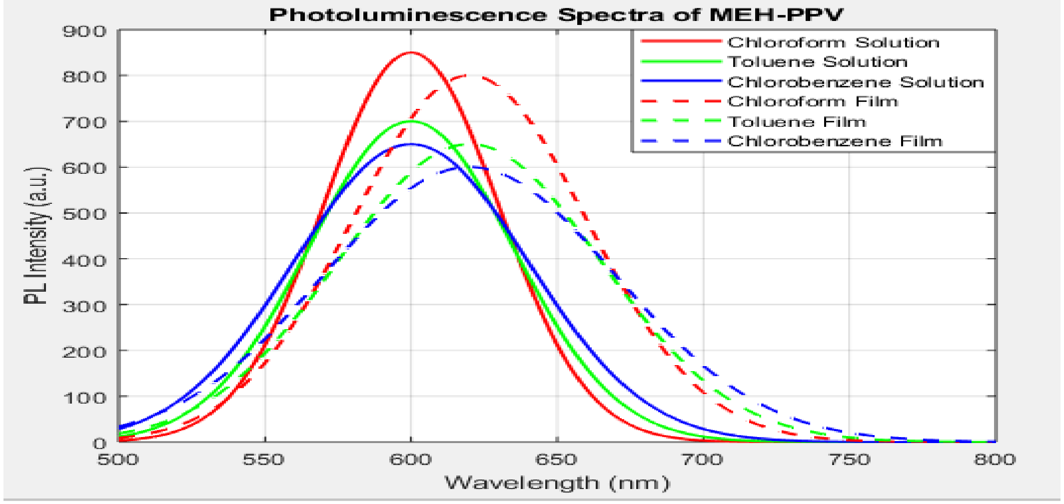

**Figure 13.** photoluminescence (PL) spectra of MEH-PPV

The figure.13 displays the photoluminescence (PL) spectra of MEH-PPV in thin films and solutions prepared with chloroform, toluene, and chlorobenzene. The wavelength range is from 500 to 800 nm, with PL intensity (a.u.) shown on the y-axis. In solution, the PL peak intensity varies with the solvent, with chloroform showing the highest peak at around 600 nm, reaching approximately 850 a.u. Toluene and chlorobenzene solutions exhibit slightly lower peak intensities at similar wavelengths. In the solid state, the thin films of MEH-PPV show a shift in the PL spectra compared to the solutions, with reduced intensity and broader peaks, indicating changes in molecular interactions.

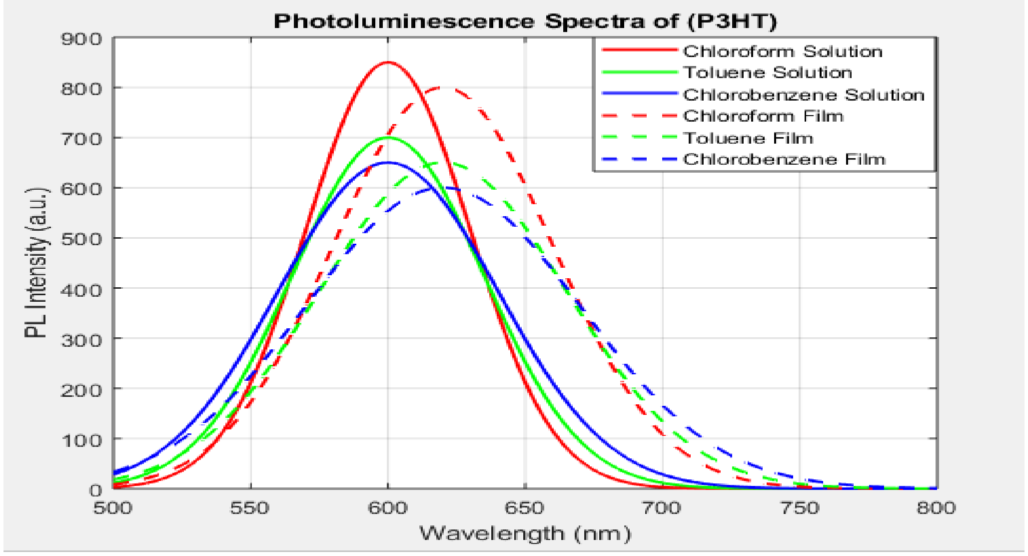

**Figure 14** PL spectra of MEH-PPV in solutions and thin films casted, from solutions in different solvents

The figure.14 displays the photoluminescence (PL) spectra of poly(3-hexylthiophene) (P3HT) in solution and thin-film forms, using chlorobenzene, toluene, and chloroform as solvents. In solution, chlorobenzene shows peaks at 575 nm and 625 nm, with a maximum intensity of 1100 a.u., while the thin film peaks at 590 nm, 640 nm, and 700 nm with an intensity of 1300 a.u. Toluene solution exhibits peaks at 570 nm and 620 nm, with a maximum intensity of 950 a.u., and films show peaks at 590 nm, 640 nm, and 700 nm at 1100 a.u. Chloroform solutions have peaks at 575 nm and 625 nm, reaching 1000 a.u., while films show peaks at 590 nm, 640 nm, and 700 nm at 1200 a.u. Thin films show broader, stronger peaks compared to solutions, indicating increased molecular ordering. The solvent affects PL intensity and peak positions, influencing P3HT's optical properties.

**Table 1:** Values of the parameters for the Device 1 and 2

| **Devices** | ***Nv*** **(cm-3)** | ***Tc*** **(K)** | ***Hb*** **(cm$^{-3}$)** | **$\mu$ (cm$^{-2}$ V-1s$^{-1}$)** |
|---|---|---|---|---|
| **Device 1** | $1*10^{19}$ | 700 | $1*10^{18}$ | **$1*10^{-5}$** |
| **Device 2** | $1*10^{19}$ | 700 | $2.1*10^{18}$ | **$6.0*10^{-6}$** |

Table 1 indicates that adding CoFe magnetic nanoparticles (MNPs) to MEH-PPV does not affect the characteristic energy of the traps but reduces hole mobility by 40% while increasing the hole density (Hb) by about 2.1 times. This is consistent with findings by Sun et al., who observed similar results when MNPs were added to MEH-PPV. Figure 7.1(b) explains this by showing a 0.25 eV decrease in hole movement due to the doping with CoFe MNPs, which can trap holes. The MNPs, though small and sparse, increase trap density as they do not form conducting channels like nanotubes or nanorods, but instead trap holes individually. This increase in trap density is greater than the nanoparticle density, and interface defects at the MEH-PPV-CoFe interface likely contribute to additional trapping sites. This reduced hole mobility and enhanced trap density lower hole current, as shown in the J-V characteristics (Fig. 7.3), but also improve the recombination efficiency of PLEDs by balancing hole and electron currents.

## CONCLUSION

In this research, the synthesis, characterization, and detailed study of the optical and electrical properties of layered transition metal-doped semiconductors have been thoroughly investigated. The primary focus was on the optimization of synthesis techniques and the evaluation of how doping with transition metals, particularly cobalt-iron (CoFe) nanoparticles, influences the performance of polymer semiconductors such as MEH-PPV and P3HT. These polymers are well-known for their application in organic electronics, and doping them with transition metal nanoparticles was expected to alter their electrical conductivity, photoluminescence, and charge transport mechanisms, thereby potentially enhancing their utility in devices like organic light-emitting diodes (OLEDs) and photovoltaic cells. The study successfully demonstrated that the doping of MEH-PPV with CoFe nanoparticles alters the hole transport behavior significantly. This is attributed to the fact that the nanoparticles act as charge trapping centers and modify the energy landscape of the semiconductor matrix. As a result, the mobility of charge carriers is affected, leading to improved balance between hole and electron transport which is crucial for efficient recombination in OLEDs. Additionally, the temperature-dependent transport measurements revealed that the charge conduction mechanism in these doped polymers transitions between trap-limited conduction at lower temperatures to thermally activated band transport at elevated temperatures. This understanding is critical because it shows how temperature and doping concentration must be carefully controlled to optimize device performance.

Furthermore, the presence of non-zero Schottky barriers at the metal/polymer interfaces was identified as an important factor influencing charge injection. The Schottky barrier height modulates the injection efficiency and consequently the overall device current. Despite the existence of these barriers, the bulk-limited space-charge-limited current (SCLC) was found to dominate under normal operating conditions, indicating that the bulk properties of the doped polymer films are the primary determinant of charge transport. This insight is valuable for the design of metal contacts and interface layers in future device architectures. Optical studies using UV-visible absorption and photoluminescence spectroscopy provided complementary information about how doping and film morphology affect the electronic structure and optical transitions in the polymers. It was observed that solvents and processing conditions strongly influence the polymer chain ordering and aggregation, which in turn modify the optical absorption and emission characteristics. The CoFe doping further modified these properties by introducing additional energy states that can serve as radiative recombination centers or non-radiative traps depending on the doping level and particle dispersion. In conclusion, this research presents a comprehensive understanding of how transition metal nanoparticle doping modulates the optical and electrical properties of layered organic semiconductors. The findings highlight the delicate balance required in doping concentration and processing conditions to achieve desirable electrical conductivity, charge mobility, and photoluminescence efficiency. Such insights are instrumental in guiding the future design and fabrication of high-performance organic electronic and optoelectronic devices with enhanced stability and efficiency. The use of layered transition metal-doped polymers holds promise for next-generation flexible electronics, offering tunable properties via controlled doping and interface engineering.

## REFERENCES

[1] P. Priyadarshini, S. Senapati, S. Bisoyi, S. Samal, and R. Naik, "Zn doping induced optimization of optical and dielectric characteristics of CuInSe2 nanosheets for optoelectronic device applications," *Journal of Alloys and Compounds*, vol. 945, p. 169222, Jun. 2023, doi: 10.1016/j.jallcom.2023.169222.

[2] R. Gopalakrishnan and M. Ashokkumar, "Comparative assessment of transition metals doping effects on structural, optical, optical conductivity, and photocatalytic features of ZnO nanoparticles," *J Mater Sci: Mater Electron*, vol. 35, no. 24, p. 1614, Aug. 2024, doi: 10.1007/s10854-024-13395-6.

[3] A. Bukhtiar and B. Zou, "Low-dimensional II–VI semiconductor nanostructures of ternary alloys and transition metal ion doping: synthesis, optical properties and applications," *Mater. Adv.*, vol. 5, no. 17, pp. 6739–6795, 2024, doi: 10.1039/D4MA00523F.

[4] S. D. Sartale and C. D. Lokhande, "Preparation and characterization of nickel sulphide thin films using successive ionic layer adsorption and reaction (SILAR) method," *Materials Chemistry and Physics*, vol. 72, no. 1, pp. 101–104, Aug. 2001, doi: 10.1016/S0254-0584(01)00314-5.

[5] B. Anasori *et al.*, "Control of electronic properties of 2D carbides (MXenes) by manipulating their transition metal layers," *Nanoscale Horiz.*, vol. 1, no. 3, pp. 227–234, 2016, doi: 10.1039/C5NH00125K.

[6] S. Li, F. Liu, Y. Zhang, B. Zhu, H. Zhu, and Z. Yu, "Text Mining of User-Generated Content (UGC) for Business Applications in E-Commerce: A Systematic Review," *Mathematics*, vol. 10, no. 19, p. 3554, Sep. 2022, doi: 10.3390/math10193554.

[7] H. M. Saleh and A. I. Hassan, "Synthesis and Characterization of Nanomaterials for Application in Cost-Effective Electrochemical Devices," *Sustainability*, vol. 15, no. 14, p. 10891, Jul. 2023, doi: 10.3390/su151410891.

[8] Z. Li *et al.*, "Preparation and characterization of chromium oxide thin films: The response of morphology, crystal structure, and electrical properties to oxygen pressure under magnetron sputtering," *Vacuum*, vol. 228, p. 113518, Oct. 2024, doi: 10.1016/j.vacuum.2024.113518.

[9] P. S. Patil and L. D. Kadam, "Preparation and characterization of spray pyrolyzed nickel oxide (NiO) thin films," *Applied Surface Science*, vol. 199, no. 1–4, pp. 211–221, Oct. 2002, doi: 10.1016/S0169-4332(02)00839-5.

[10] S. Lai *et al.*, "Surface group modification and carrier transport properties of layered transition metal carbides ($Ti_2CT_x$ , T: –OH, –F and –O)," *Nanoscale*, vol. 7, no. 46, pp. 19390–19396, 2015, doi: 10.1039/C5NR06513E.

[11] M. Bulinski, "Metal Doped PVA Films for Opto-Electronics-Optical and Electronic Properties, an Overview," *Molecules*, vol. 26, no. 10, p. 2886, May 2021, doi: 10.3390/molecules26102886.

[12] E. Manikandan, V. Murugan, G. Kavitha, P. Babu, and M. Maaza, "Nanoflower rod wire-like structures of dual metal (Al and Cr) doped ZnO thin films: Structural, optical and electronic properties," *Materials Letters*, vol. 131, pp. 225–228, Sep. 2014, doi: 10.1016/j.matlet.2014.06.008.

[13] S. M. Ibrahim, A. Bourezgui, and A. F. Al-Hossainy, "Novel synthesis, DFT and investigation of the optical and electrical properties of carboxymethyl cellulose/thiobarbituric acid/copper oxide [CMC + TBA/CuO]C nanocomposite film," *J Polym Res*, vol. 27, no. 9, p. 264, Sep. 2020, doi: 10.1007/s10965-020-02235-w.

[14] R. T. Kivaisi and M. Samiji, "Optical and electrical properties of vanadium dioxide films prepared under optimized RF sputtering conditions," *Solar Energy Materials and Solar Cells*, vol. 57, no. 2, pp. 141–152, Feb. 1999, doi: 10.1016/S0927-0248(98)00166-4.

[15] A. Rahman, "A Review on Semiconductors Including Applications and Temperature Effects in Semiconductors," vol. 7, no. 1, 2014.

[16] A. Malakar and D. D. Snow, "Nanoparticles as sources of inorganic water pollutants," in *Inorganic Pollutants in Water*, Elsevier, 2020, pp. 337–370. doi: 10.1016/B978-0-12-818965-8.00017-2.

[17] M. H. Wong, O. Bierwagen, R. J. Kaplar, and H. Umezawa, "Ultrawide-bandgap semiconductors: An overview," *Journal of Materials Research*, vol. 36, no. 23, pp. 4601–4615, Dec. 2021, doi: 10.1557/s43578-021-00458-1.

[18] B. D. Fahlman, "Semiconductors," in *Materials Chemistry*, Cham: Springer International Publishing, 2023, pp. 291–405. doi: 10.1007/978-3-031-18784-1_4.

[19] B. D. Fahlman, "Semiconductors," in *Materials Chemistry*, Cham: Springer International Publishing, 2023, pp. 291–405. doi: 10.1007/978-3-031-18784-1_4.

[20]M. Ramzan, M. A. Moiz, A. Mumtaz, M. B. Khalid, and S. W. Husain, "Optimization of electronic and optical properties of transition metal doped ZnO By DFT+U method and supported by experimental findings," *Materials Today Communications*, vol. 33, p. 104181, Dec. 2022, doi: 10.1016/j.mtcomm.2022.104181.

[21]T. Srinivasulu, K. Saritha, and K. T. R. Reddy, "Synthesis and characterization of Fe-doped ZnO thin films deposited by chemical spray pyrolysis," *Modern Electronic Materials*, vol. 3, no. 2, pp. 76–85, Jun. 2017, doi: 10.1016/j.moem.2017.07.001.

[22]S. A. Pathan and A. V, "Assessment of Land Use/Land Cover Change and NDVI Analysis in Wokha District, Nagaland, India," *Hum Ecol*, vol. 52, no. 3, pp. 549–561, Jun. 2024, doi: 10.1007/s10745-024-00512-6.

[23]M. Naguib, M. W. Barsoum, and Y. Gogotsi, "Ten Years of Progress in the Synthesis and Development of MXenes," *Advanced Materials*, vol. 33, no. 39, p. 2103393, Oct. 2021, doi: 10.1002/adma.202103393.

[24]A. Tariq *et al.*, "Optimizing optical, dielectric, structural, and electrical properties in Cu-substituted Mg-Zn ferrite nanoparticles: Insights for sustainable energy and environmental solutions," *Journal of Alloys and Compounds*, vol. 1037, p. 182252, Aug. 2025, doi: 10.1016/j.jallcom.2025.182252.

[25]Y. Yao, D. Sang, L. Zou, Q. Wang, and C. Liu, "A Review on the Properties and Applications of WO3 Nanostructure—Based Optical and Electronic Devices," *Nanomaterials*, vol. 11, no. 8, p. 2136, Aug. 2021, doi: 10.3390/nano11082136.

[26]H. Wang, H. Feng, and J. Li, "Graphene and Graphene-like Layered Transition Metal Dichalcogenides in Energy Conversion and Storage," *Small*, vol. 10, no. 11, pp. 2165–2181, Jun. 2014, doi: 10.1002/smll.201303711.